



Limitations of homogeneous and segmented single-crystal compact TEM₀₀-mode Ho³⁺:YAG laser resonators

Katharina Goth^{1,2} · Marius Rupp^{1,2} · Michael Griesbeck¹ · Madeleine Eitner¹ · Marc Eichhorn^{1,2} · Christelle Kieleck¹

Received: 27 March 2023 / Accepted: 30 April 2023 / Published online: 21 May 2023
© The Author(s) 2023

Abstract

We present investigations on output power limitations of near-diffraction-limited compact Ho³⁺:YAG laser resonators employing a homogeneous or segmented laser crystal. An approach for designing a segmented crystal is presented. Maximum output powers of 57.6 W and 51.9 W are reached with the homogeneous and segmented crystal, respectively, resulting in pulse energies of 1.14 mJ and 1.04 mJ at a repetition rate of 50 kHz in Q-switched operation. Interferometric experiments are conducted to derive the radial temperature profile for both crystals. Simulations based on a split-step beam propagation method are used to model the longitudinal temperature gradient in both crystals.

Keywords Ho³⁺:YAG · Segmented crystal · Q-switching · Thermal lensing

1 Introduction

Applications of lasers in the 2 μm range are versatile and include medical surgery, remote sensing, material processing, and nonlinear conversion into the mid-infrared range [1–4]. Holmium-doped yttrium-aluminum-garnet (Ho³⁺:YAG) is especially suitable for the generation of 2 μm laser light, mainly due to the following reasons: Firstly, Ho³⁺:YAG crystals can be efficiently pumped by commercially

available Tm³⁺-doped fiber lasers at 1908 nm which leads to a small quantum defect and therefore a low heat generation. Secondly, YAG has a high thermal conductivity which increases the removal of heat from the crystal. Thirdly, Ho³⁺ has a long upper state lifetime, e.g. in comparison to Nd³⁺ and Yb³⁺ [5], which is especially useful for Q-switched operation since a long upper state lifetime provides a good energy storage capacity resulting in high extraction efficiencies.

In Ho³⁺:YAG lasers, thermal lensing is the main mechanism for power limitations in TEM₀₀ mode of operation. Due to the quasi-three-level nature of Ho³⁺:YAG, high pump intensities, which are usually realized by using small pump diameters, have to be generated in order to create a high inversion [5]. In contrast to four-level lasers where the lower laser level is unpopulated and therefore an inversion is created even for low pump intensities, the lower laser level is thermally populated in quasi-three-level lasers resulting in a higher threshold that has to be overcome prior to laser operation.

In recent years, several high-output-power Ho³⁺:YAG lasers have been presented. For example, Lippert et al. have shown an output power of 42 W with a double-pass pumping scheme in 2010 [6]. In 2019, Chen et al. have presented a resonator with two Ho³⁺:YAG crystals reaching an output power of 55.6 W [7]. Even higher output powers have been generated by using two pump lasers in a dual-end pumping scheme. This pumping scheme has the big advantage that the longitudinal temperature gradient is decreased since the

✉ Katharina Goth
katharina.goth@iosb-extern.fraunhofer.de

Marius Rupp
marius.rupp@iosb-extern.fraunhofer.de

Michael Griesbeck
michael.griesbeck@iosb.fraunhofer.de

Madeleine Eitner
madeleine.eitner@iosb.fraunhofer.de

Marc Eichhorn
marc.eichhorn@iosb.fraunhofer.de

Christelle Kieleck
christelle.kieleck@iosb.fraunhofer.de

¹ Fraunhofer IOSB (Institute of Optronics, System Technologies and Image Exploitation), Gutleuthausstraße 1, 76275 Ettlingen, Germany

² Institute of Control Systems, Karlsruhe Institute of Technology, Fritz-Haber-Weg 1, 76131 Karlsruhe, Germany

pump light is incident onto the crystal from both end facets. This is also achieved with double-pass pumping, but the effect is smaller since the back reflected pump light is less intense compared to the incident pump light. Furthermore, the possibility to place the crystal in the center of the resonator leads to a wider stability range. With this design, output powers over 100 W with a good beam quality have been demonstrated [8, 9]. However, these designs have used long laser rods increasing the number of ions contributing to laser operation which is an explanation for the high output powers. A disadvantage of these long laser rods is the inevitable increase in resonator length which decreases the compactness of the system.

In contrast to dual-end pumping, another approach for decreasing the longitudinal temperature gradient and the resulting thermal stresses in the crystal is the use of crystals which consist of segments with different doping concentrations. Relative to the direction of incidence of the pump beam, these segmented crystals have a lower doping concentration at the front and a higher doping concentration at the end of the crystal. While a homogeneously doped crystal experiences a high temperature peak at the front of the crystal resulting from an absorption peak according to the Beer-Lambert law, a segmented crystal absorbs less pump light in the lower-doped segment at the front of the crystal and, thus, transmits more pump light to the back of the crystal. Compared to the homogeneously doped crystal, this leads to a more uniform temperature profile along the crystal axis, resulting from the decreased temperature at the front of the crystal and an increased temperature at the end of the laser rod. Segmented crystals have already been used in high-power Nd³⁺:YAG lasers [10–12] and were shown to allow for an increased output power. In these reports, a higher pump power could be used since the maximum temperature and thermal stresses in the segmented crystal have been considerably reduced which allowed for a higher output power. Shen et al. have further shown in their experiments that a segmented crystal reduces the refractive power of the thermal lens [13]. Evangelatos et al. have reported a significantly improved beam profile with a segmented Nd³⁺:YAG crystal [14]. These promising results and the lack of research on the use of segmented crystals in Ho³⁺:YAG lasers encouraged us to investigate a segmented Ho³⁺:YAG crystal.

The goal of this work is to investigate the opportunities and limitations of a segmented crystal in a compact single-end-pumped resonator, compare the results to a corresponding resonator with a homogeneous crystal, and find the output power limits for both crystals. At first, an approach for designing the segmented crystal is presented. The subsequent section shows the characterization of the experimentally optimized resonators with both the segmented and the homogeneous crystal. An interferometric investigation of the thermal lens and a precise thermal simulation of

both crystals is used to get a deeper understanding of the radial and longitudinal temperature gradients in the crystals. Finally, the results are discussed and compared to previously published experiments, with a particular focus on the possible differences between them.

2 Design of segmented Ho³⁺:YAG crystal

2.1 Optimization of segment lengths and doping concentration

As has been shown by Wilhelm et al. in [11], the on-axis temperature of an end-pumped crystal is significantly reduced when diffusion bonded crystals consisting of segments with increasing doping concentrations are used. To find the optimum doping concentrations and segment lengths, different approaches have been presented in [11] which all have led to different segmented crystals. In one of the presented optimization criteria, the optimum absorption coefficient that leads to a constant absorption per unit length is approximated by the absorption coefficient of the segmented crystal. Another optimization criterion minimizes the variance of the resulting temperature distribution and the last one minimizes the temperature peaks of the distribution. In a crystal with N segments with lengths L_i ($i = 1, \dots, N$) and absorption coefficients α_i ($i = 1, \dots, N$) and a double-pass pumping scheme, the on-axis temperature distribution in the n -th segment is described by

$$T(z) \propto \alpha_n \cosh \left[\sum_{i=n}^N \alpha_i L_i - \alpha_n \cdot \left(z - \sum_{i=1}^{n-1} L_i \right) \right],$$

for $L_1 + \dots + L_{n-1} \leq z < L_1 + \dots + L_n$,

when the axial heat transport is neglected.

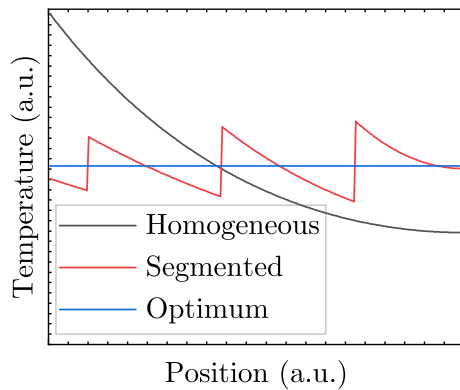
Here, we present a slightly different approach. It is based on the idea that in an ideal crystal with longitudinally varying absorption coefficient, the absorption per unit length and therefore the temperature T_{opt} is constant along the crystal axis. The temperature distribution $T(z)$ of the segmented crystal is optimized such that the difference between the temperature distribution and the optimum temperature is minimized. Hence, the function

$$f(\alpha_1, \dots, \alpha_n, L_1, \dots, L_n) = \int_0^L (T(z) - T_{\text{opt}})^2 dz,$$

where L is the total length of the crystal, has to be minimized. Furthermore, the following constraints are included in the optimization: Firstly, the segmented crystal is required to have the same absorption times length product as a homogeneous reference crystal. Secondly, four segments are used since Wilhelm et al. have shown that the expected

Table 1 Lengths and relative doping concentrations of the designed segmented crystal with regard to the homogeneous crystal

Segment number	1	2	3	4
Length share	0.1	0.3	0.3	0.3
Doping concentration	0.5	0.7	1	1.6


Fig. 1 Theoretical temperature distribution of homogeneous, optimum, and segmented crystal neglecting axial heat transport

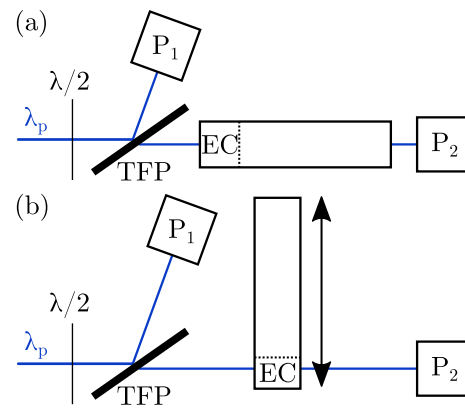
improvement for more segments is only small [15]. Thirdly, three doping concentrations are fixed due to availability of already existing crystals.

Under these constraints, the lengths and doping concentrations of the resulting segmented crystal are given in Table 1 in relation to the homogeneous reference crystal. Figure 1 shows the expected temperature distribution for the homogeneous, segmented, and optimum crystal.

2.2 Measurement of doping concentration

In order to verify the composition of the fabricated segmented crystal, the absorption as a measure for the doping concentration is determined. Figure 2a shows the measurement of the longitudinal absorption. Polarized pump light with $\lambda_p = 1908$ nm is attenuated by a combination of a half-wave plate and a thin-film polarizer (TFP) and transmitted longitudinally through the laser crystals. Since both crystals are anti-reflection (AR) coated, reflections at the end facets are neglected and the absorption coefficient can be determined from the incident and the transmitted power. While the power monitor P_1 allows for the calculation of the incident power on the crystal, the transmitted power through the crystal is measured using power meter P_2 .

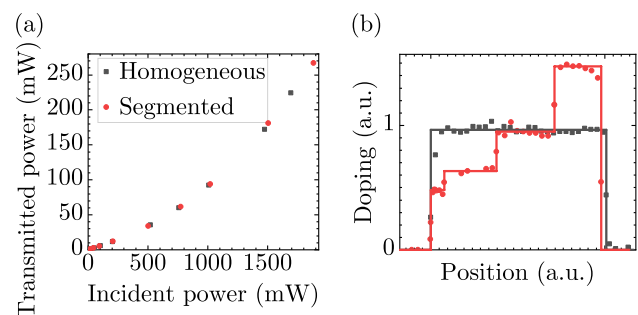
For the determination of the doping concentration, the transmitted power P_2 through the crystal is measured perpendicular to the crystal axis (see Fig. 2b). The power incident on


Fig. 2 **a** Measurement of longitudinal absorption. **b** Experimental setup for the determination of the doping concentration

the crystal is kept in the mW-regime to avoid saturation effects. Since the crystal has a cylindrical shape where the surface is not AR coated, reflections are considered by measuring the transmitted power $P_{2,E}$ behind the undoped and non-absorbing end cap (EC) which is attached at the front of the crystals. Also, the influence of refraction at the curved interface has to be considered but was shown to be negligible in [16]. By measuring the transmitted power behind the doped segments and applying the correction becoming necessary due to the reflection at the curved surface, the doping concentration is calculated from the transmitted power, the absorption cross section, and the geometry of the sample. By using the Beer-Lambert law, the transmitted power behind a doped piece of the crystal is

$$P_2 = P_1 \cdot \frac{P_{2,E}}{P_{1,E}} \cdot \exp(-\alpha \cdot d),$$

where $P_{1,E}$ and $P_{2,E}$ is the power measured with an illuminated end cap and d is the diameter of the crystal. The doping concentration is finally derived from the absorption coefficient, the absorption cross section of Ho³⁺-ions in YAG as well as structural properties of the host material.


Fig. 3 **a** Longitudinal transmission through the crystals (black: homogeneous, red: segmented). **b** Doping concentrations of homogeneous (black) and segmented (red) crystal

The experimental data shows that the longitudinal transmission through the crystal is very similar for the homogeneous and the segmented crystal (see Fig. 3a). This means that both crystals experience the same total absorption efficiency and therefore, the doping concentration averaged over the crystal length is the same. For higher input powers, in both cases the transmission increases disproportionately which results from the saturation of absorption. Figure 3b shows the relative doping concentrations along the crystal axis for the homogeneous (black) and the segmented (red) crystal. The measurements confirm that both the segment lengths and doping concentrations are in accordance with the design.

3 Laser performance of the two crystals

3.1 Experimental setup

Figure 4 shows the experimental setup. The $^5I_8 \rightarrow ^5I_7$ transition of the $\text{Ho}^{3+}:\text{YAG}$ crystal is pumped by a commercially available 100 W, 1908 nm Tm^{3+} -doped fiber laser with a beam quality of $M^2 < 1.1$. The pump beam is focused by a Galilean telescope (L_1 and L_2) with adjustable lens distance. The input coupling (IC) mirror couples the pump light into the resonator and is highly reflective (HR) at 1908 nm and for the s-polarized fraction of the 2090 nm light and highly transmissive (HT) at the p-polarized 2090 nm output. The crystals described in Sect. 2 are both mounted in copper heat sinks which are water-cooled to a temperature of 20 °C. The HR mirror on the left side of the crystal is highly reflective for both the pump and signal light resulting in a double-pass of the pump light to improve the absorption efficiency. It is plano-convex with a radius of curvature of -0.25 m. The output coupling (OC) mirror is plano-concave with a reflectivity of $R = 50\%$ and a radius of curvature of 0.3 m. Furthermore, the cavity contains an acousto-optic modulator (AOM) to enable Q-switching and an etalon (E) to select the 2090 nm line in order to make use of the strongest emission peak of $\text{Ho}^{3+}:\text{YAG}$ yielding maximum output power.

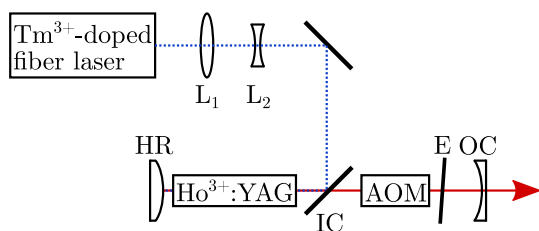


Fig. 4 Schematic architecture of the laser setup (abbreviations are explained in the text)

3.2 Comparison of the two crystals

Experimental evidence through varying mirror radii of curvature has shown that for both crystals the same mirrors have to be used to receive the optimum output power. In continuous wave operation, both lasers exhibit high slope efficiencies of 67.6 % and 66.9 % for the homogeneous and segmented crystal, respectively (see Fig. 5). One reason for the lower slope efficiency of the resonator with the segmented crystal might be that this crystal contains one highly doped segment in which upconversion processes could lead to additional losses and an increased heat generation.

The superior performance of the resonator with the homogeneous crystal with regard to maximum output power is explained with the specific position of the thermal lens inside the two crystals. Figure 6 shows a very simplified setup of a resonator of length L with a thermal lens f at a distance of d from one mirror. Following the approach of Magni [17], such a resonator is stable for $\frac{d(L-d)}{L} < f < d$ and $f > L - d$. In our experiments, the thermal lens is in the second stability range. This means that if the thermal lens moves closer to the HR mirror, the minimum focal length for which the resonator is still stable increases. As the host material YAG has a positive thermo-refractive index and the focal length of the thermal lens becomes shorter as the

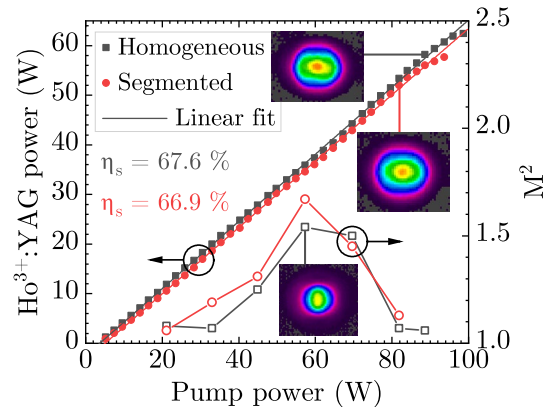


Fig. 5 a Comparison of power-power curves and beam quality factors of homogeneous (black) and segmented (red) crystal

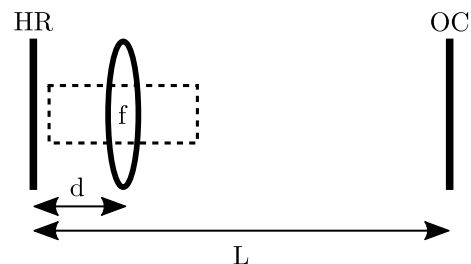


Fig. 6 Simple resonator with thermal lens

absorbed power increases, the resonator becomes unstable already for smaller absorbed pump powers. For the homogeneous crystal, the highest absorption is at the front of the crystal and therefore, the effective position of the lens tends to be near the front of the crystal. For the segmented crystal, on the other hand, the effective position of the thermal lens is rather in the middle of the crystal due to the more homogeneous absorption. Since both crystals are pumped from the center of the resonator, this means that the effective position of the thermal lens in the homogeneous crystal has a shorter distance from the OC mirror and consequently, the resonator is stable for a shorter focal length of the thermal lens, which corresponds to higher pump powers and finally results in the observed higher output power.

The beam quality factor strongly depends on the pump power. For reasons of clarity, only the beam quality factor along the vertical beam direction is shown in Fig. 5. At low pump powers of around 20 W, the beam quality is excellent since for low powers only the TEM₀₀ mode experiences enough gain. The beam quality deteriorates with increasing pump powers until it reaches a beam quality factor of around 1.55 for the resonator with the homogeneous (1.7 for the segmented) crystal at a pump power of 57 W (beam profile exemplarily shown for the resonator with the homogeneous crystal as inset). This probably results from a mode mismatch of pump and laser mode where the pump mode is considerably larger than the laser mode and therefore, also higher order modes experience gain. When the pump power is increased even further, the beam quality factor improves again resulting from an increasing size of the laser mode until mode matching is achieved at 89 W of pump power for the resonator with the homogeneous and at 82 W of pump power for the resonator with the segmented crystal. The insets of Fig. 5 show the beam profile at these pump powers for both resonators. Again, this measurement reveals a shift to higher pump powers for the resonator with the homogeneous crystal.

Figure 7 shows the residual pump power (a) and the depolarized power (b) for both resonators. In the resonator with the segmented crystal, the residual pump power is higher which might result from two factors: Firstly, a better mode matching in the homogeneous crystal leads to an improved absorption since excited states are more efficiently de-excited by stimulated emission and hence, are able to absorb photons again. Secondly, the absorption saturates in the low doped segment of the segmented crystal and therefore, results in the slightly reduced total absorption. The depolarized power is slightly smaller for the resonator with the segmented crystal for pump powers below 87 W. This is expected since the segmented crystal has been designed to have lower peak temperatures and therefore experiences fewer stress. However, this does not hold for higher pump powers since this resonator has been

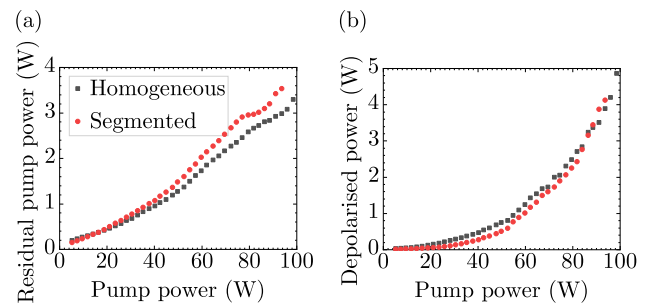


Fig. 7 Comparison of **a** residual pump power and **b** depolarization in the resonator with the homogeneous (black) and segmented (red) crystal

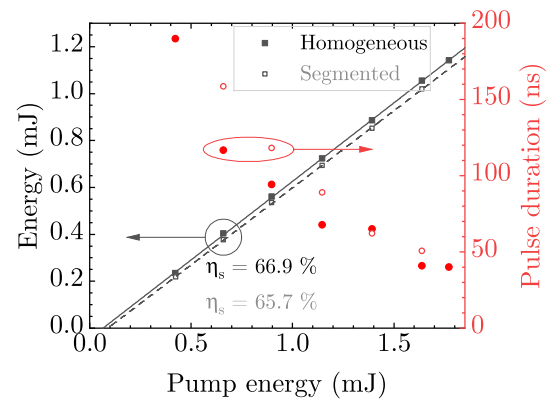


Fig. 8 Comparison of pulse energy (black) and pulse width (red) for the resonator with the homogeneous (filled symbols) and segmented crystal (empty symbols)

optimized for 82 W of pump power which explains the strong increase in depolarization for pump powers above 87 W. In contrast, the homogeneous crystal has been optimized at 89 W of pump power.

In Q-switched operation, the resonator is operated in the quasi-continuous regime at repetition rates between 25 kHz and 100 kHz. For the characterization, a medium repetition rate of 50 kHz is chosen. Figure 8 shows the pulse energy and pulse width at that repetition rate for both crystals. Due to operation in the quasi-continuous regime, the same trend is observed for the pulse energy as has been observed in continuous wave operation for the output power. The maximum pulse energies are 1.14 mJ and 1.04 mJ for the homogeneous and segmented crystal, respectively. The pulses generated involving the segmented crystal are slightly longer than those generated with the homogeneous crystal. This is attributed to a smaller inversion due to a larger pump diameter which is necessary to achieve mode matching in the segmented crystal. The minimum pulse width is 40 ns for the resonator with the homogeneous crystal and 50 ns for the segmented crystal.

Figure 9a shows the average output power over half an hour for both resonators. The output power is stable with a standard deviation of 0.1 W. Also, at these output powers excellent beam quality factors of around 1.1 are measured for both resonators. Figure 9b shows a beam quality measurement for the laser based on the segmented crystal as an example. The beam profile is slightly elliptical and the different beam waist positions of x- and y-axis indicate that the beam is astigmatic which results from two contributions. Firstly, the eigenvectors of the thermally induced stress tensor are radial and tangential due to the cylindrical shape of the crystals which leads to a refractive index change in these directions as well. This results in bifocusing when the laser mode is linearly polarized [18]. Secondly, since the pump light is coupled into the crystal with a 45° mirror the resonator is axially asymmetric resulting in different effective resonator lengths in x- and y-direction [19]. This effect becomes even more pronounced when the resonator is operated near its stability limit since then a small change in thermal lens results in a large change in mode diameter.

Figure 10 shows the pulse energy and pulse width for the optimum laser with the homogeneous crystal depending on

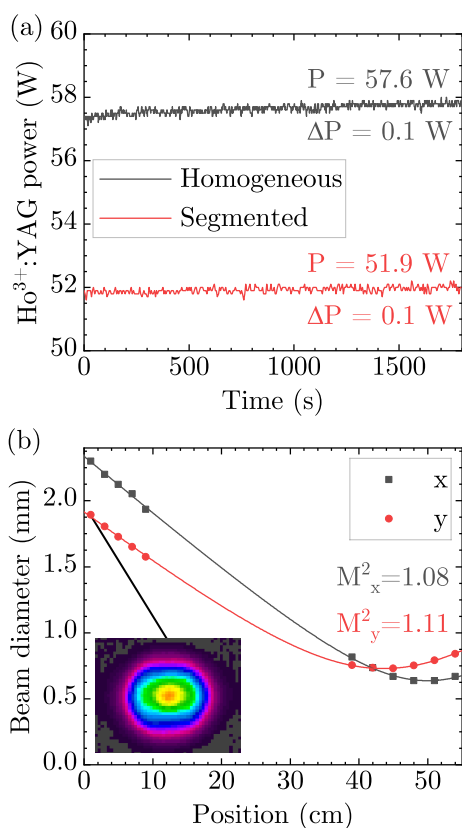


Fig. 9 **a** Comparison of long time output power for the resonators with the homogeneous (black) and segmented (red) crystal. **b** Exemplary beam quality measurement for the resonator with the homogeneous crystal at a pump power of 89 W

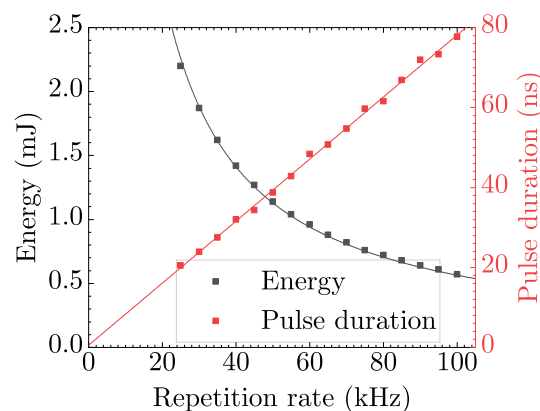


Fig. 10 Pulse energy (black) and pulse duration (red) depending on repetition rate

the pulse repetition rate. For a repetition rate of 25 kHz, a maximum pulse energy of 2.2 mJ is achieved with a pulse width of 20 ns resulting in a pulse peak power of 108 kW which, to the best of our knowledge, is the highest peak power achieved in a nearly diffraction-limited Ho³⁺:YAG crystal pumped in a double-pass configuration with a single pump laser and operated at such a high pulse repetition frequency. Higher peak powers have only been reached in Ho³⁺:YAG lasers with lower pulse repetition frequency [20] or dual-end pumping [8, 9] which increases the resonator stability since the crystal including the thermal lens can be positioned in the center of the resonator and furthermore, with this pump scheme, a steadier heat distribution along the crystal axis is expected.

4 Interferometric investigation of thermal lens

4.1 Experimental setup

To gain a deeper understanding of the thermal lens in the homogeneous and segmented crystal, an interferometer experiment is set up to investigate the thermal lens during laser operation (see Fig. 11). Light from a helium-neon laser at 633 nm is shaped by two lenses such that a focus is generated in a distance of the focal length of the HR mirror. It then passes a polarizing beam splitter (PBS) and is circularly polarized by a quarter-wave plate. When it passes the HR mirror, it is collimated to a beam diameter larger than 5 mm. In the following, it is exploited that the laser crystals are not AR coated for 633 nm light and consequently, there are reflexes from the front and the back surface of the crystal which interfere with each other. Both reflexes pass the quarter-wave plate again resulting in a linear polarization rotated by 90° with respect to the incoming light and are

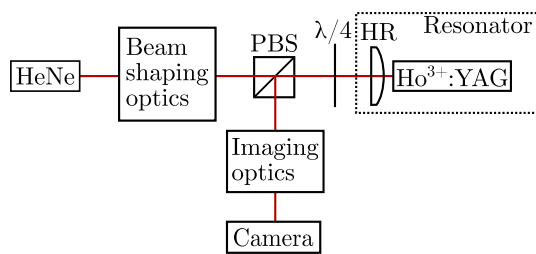


Fig. 11 Interferometer setup for thermal lens investigations

consequently reflected at the PBS. An aperture is inserted within the distance of the focal length of the HR mirror and used to spatially filter the reflections from the Ho³⁺:YAG crystal and the HR mirror. An image of the crystal is generated on a CCD camera with an imaging lens with a focal length of $f = 30$ cm.

4.2 Interferograms and derived temperature profiles

As mentioned before, the interference pattern arises from an optical path difference between the reflected light at the front and the back of the crystal. The optical path difference Δs of the two beams is

$$\Delta s = 2n(r)L,$$

where $n(r)$ is the radially varying refractive index due to the pump light absorption and L is the length of the crystal. Both the temperature gradient in the crystal and mechanical stresses result in a change in refractive index. Therefore

$$n(r) = n_0 + \Delta n(r)_T + \Delta n(r)_\epsilon,$$

where n_0 is the refractive index without pump light absorption, $\Delta n(r)_T$ is the refractive index variation due to the thermo-optic effect, and $\Delta n(r)_\epsilon$ is the refractive index variation due to the elasto-optic effect [18]. Since in Ho³⁺:YAG a large contribution to the refractive index variation results from the thermo-optic effect, only this effect is considered for estimating the radial temperature distribution. Furthermore, end face bulging influences the interferograms, but is neglected since this effect is assumed to be rather small as well. From this and the wavelength λ of the helium-neon laser, it is concluded that the refractive index difference between two interference fringes is

$$\Delta n = \frac{\lambda}{2L},$$

which, in combination with the thermo-optic coefficient of YAG $dn/dT = 9 \cdot 10^{-6} \text{K}^{-1}$, results in a temperature difference of

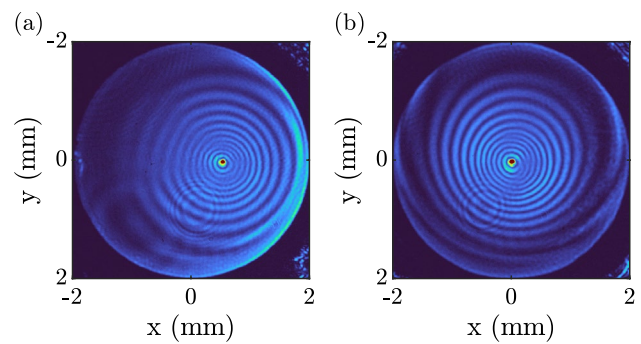


Fig. 12 Interferogram at 89 W of pump power for homogeneous **a** and at 82 W of pump power for segmented **b** crystal

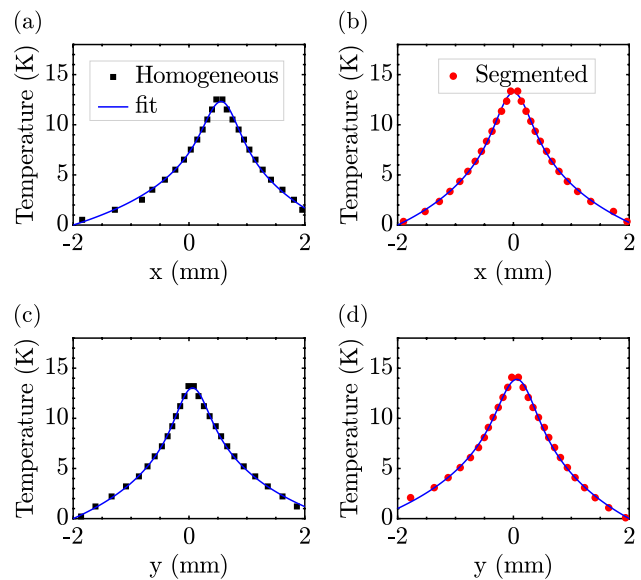


Fig. 13 Averaged temperature gradient along x-direction for homogeneous **a** and segmented **b** crystal and along y-direction for homogeneous **c** and segmented **d** crystal with respect to the temperature at the edge of the rod

$$\Delta T = \frac{\Delta n}{dn/dT} \approx 1 \text{ K}. \quad (1)$$

Figure 12 shows the resulting interferograms of the homogeneous crystal at 89 W of pump power and of the segmented crystal at 82 W of pump power. Both interferograms show a similar number of interference fringes which indicates that the axially averaged temperature gradient is in a similar range. By locating the positions of the interference fringes in x- and y-direction, temperature profiles with respect to the edge temperature of the rod are derived along these directions, which are shown in Fig. 13. For Gaussian end-pumped crystals, the radial temperature distribution derived by Innocenzi [21] is given by

$$T(r) = A \cdot \left(\ln \left(\frac{b^2}{r^2} \right) - E_1 \left(\frac{2r^2}{\omega_p^2} \right) \right) \quad (2)$$

where A is proportional to the peak temperature, b is the rod radius, E_1 is the exponential integral function, and ω_p is the pump radius. This function has slightly been modified to account for a non-centrosymmetric profile. The temperature difference between the peak and the crystal edges is approximately 12.7 K for the homogeneous and 13.5 K for the segmented crystal. This means that both crystals experience a similar thermal lens. This has been expected since both crystals have been designed to have the same total absorption and therefore should result in a similar longitudinally averaged temperature distribution.

To get a better understanding of the longitudinal temperature gradient, a homemade simulation is used.

5 Simulation results

The simulation used in this section is presented in greater detail by Rupp et al. in [22]. The general approach to model a laser resonator is based on the propagation of the electromagnetic fields with a split-step beam propagation method. In between the propagation steps, the laser crystal as well as other optical elements transform the field. In the laser crystal the absorption, gain, and heat load is calculated. The resulting temperature profile can be solved numerically with a 3D finite difference method, resulting in a highly spatially resolved temperature distribution of the crystal. Consequently, the model also takes into account thermal effects like thermal lensing and birefringence.

Both resonators presented in Sec. 3.2 are simulated. Figure 14 exemplarily shows the experimental and simulated power-power curve and beam quality factor in the horizontal

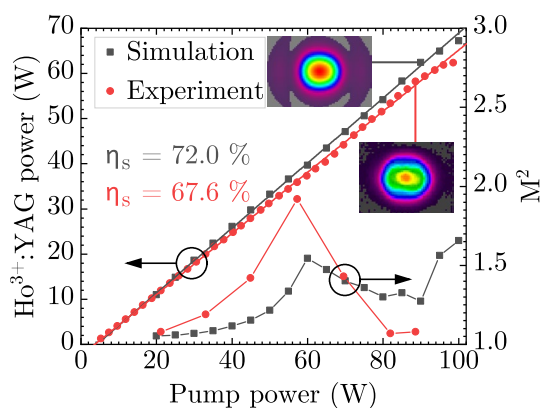


Fig. 14 Comparison of simulated (black) and experimental (red) output power and beam quality factor M^2 for the resonator with the homogeneous crystal

direction depending on the pump power for the resonator with the homogeneous crystal. The simulated and experimentally observed beam profiles are shown in the inset of Fig. 14 for a pump power of about 90 W. The slightly more elliptical beam profile observed in the experiment probably results from the axial asymmetry introduced by the inclined mirror that is used to couple the pump light into the resonator which has not been considered in the simulation. The slope efficiency and output power in the experiment is slightly lower compared to the simulation (67.6 % compared to 72.0 %). The difference in slope efficiency could result from additional losses, e.g. imperfect AR coatings, which have not been taken account in the simulation. Furthermore, the experimental beam quality factor shows a larger variation over the measurement range but the course of both curves is similar showing an excellent beam quality factor for lower pump powers, an increased beam quality factor for pump powers around 60 W, and again an excellent beam quality factor around 80 W to 90 W. The simulation of the resonator involving the segmented crystal shows a slightly lower slope efficiency of 70.3 % which agrees well with the experimental observation.

As mentioned above, the simulation data allows for the evaluation of the temperature distribution in the crystals. This is used to understand how the on-axis temperature profiles of the different crystals differ. Figure 15 shows the simulated temperature profiles for the homogeneous (black), segmented (red), and for an optimized segmented (blue) crystal. The pump light is incident onto the crystal from the left. The homogeneous crystal experiences a large temperature gradient along the crystal axis with the highest temperature being reached near the front of the crystal. The strong decrease in temperature at the front side of the crystal results from the axial heat transport into the undoped end cap. In contrast to this, the temperature gradient is smaller for the segmented crystal and the highest temperature is reached

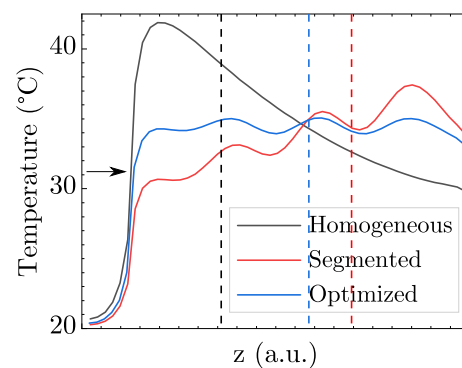


Fig. 15 Simulated temperature along crystal axis for **a** homogeneous crystal, **b** segmented crystal, and **c** optimized segmented crystal. The arrow shows the direction of the pump light. The dotted lines indicate the effective position of the thermal lens

near the end of the crystal. This supports our hypothesis that the two resonators mainly differ in the position of the thermal lens since the center of the temperature distribution is closer to the front of the crystal in case of the homogeneous crystal. The effective position of the thermal lens in the crystals is indicated as dotted line in Fig. 15. In comparison to Fig. 1, the temperature distribution of the segmented crystal experiences a larger gradient. This deviation is attributed to the fact that for the design of the segmented crystal, very simplified assumptions have been made. Another difference is that the numerical simulation includes axial heat transport which has been neglected during the design of the segmented crystal.

It needs to be mentioned here that despite the smaller temperature gradient in the segmented crystal, no higher output power and slope efficiency are reached which could result from the temperature distribution which has not been as steady as designed. To test whether an optimized segmented crystal could lead to an improved output power, a further segmented crystal has been designed and simulated (see Table 2). Although the temperature distribution of that crystal in Fig. 15 shows the smallest gradient, this design does not surpass the performance of the homogeneous crystal as well. Consequently, the simulation confirms that for the compact design presented in this report, the homogeneous crystal is the preferable choice.

6 Discussion and conclusion

In the previous sections, it has been shown that for our purposes the use of a segmented Ho³⁺:YAG crystal does neither lead to an increase in output power nor to an improved beam quality which is in contrast to previous findings mentioned in literature for Nd³⁺-doped lasers. Reasons for this will be discussed in the following section.

At first, the power limitation of this compact resonator will be discussed. By using a pump telescope with a variable pump diameter, mode matching is ensured while increasing the pump power, which is known to be crucial for single-transverse-mode operation. In a resonator with a fixed length and fixed mirror curvatures, the laser mode size depends on the pump intensity since this defines the thermal lens. In mode matched operation, the pump mode diameter equals the laser mode diameter within the crystal and therefore,

the pump power must be adapted. Conversely, this means that for each given pump power, there is one single solution where the pump and laser diameter match each other. As the thermal lens approaches the resonator stability limit, the size of the laser mode increases strongly and, thus, varies strongly along the crystal axis. This strong variation leads to difficulties in reaching mode matched operation. Hence, in such a design the maximum output power is limited and we believe, that we have reached this limit for the design presented in this paper.

However, in the last decades some research groups reported about an increased output power, weaker thermal lensing, and an improved beam quality with the use of segmented crystals [10, 11, 13, 14] or even gradient-doped crystals [23]. To understand these observations, a closer look has to be taken at the laser crystals used in these experiments and the exact operation conditions. In all these reports, the laser active ion has been Nd³⁺ in combination with YAG or yttrium orthovanadate (YVO₄) hosts. In such laser crystals, there is usually a large quantum defect, since they are generally diode-pumped at 808 nm and 888 nm, and emit at 1064 nm and 1342 nm, respectively. In contrast to this, the quantum defect is considerably smaller for Ho³⁺:YAG emitting at 2090 nm while being pumped at 1908 nm. The large quantum defect of the lasers employing Nd³⁺ leads to high temperature peaks and, consequently, high mechanical stresses in these laser crystals. Maximum on-axis temperatures between 137 °C [13] and 350 °C [10] have been reported. Further, some of these lasers have been designed to operate at very high pump powers (e.g. 750 W in [10]) independent of the resulting beam quality. Of course, the operation at high pump powers inevitably brings the crystal closer to its fracture limit. However, these conditions are very different compared to the operation conditions presented in our experiments where the simulated peak temperature of the homogeneous crystal has only been 42 °C and a moderate pump power below 100 W has been used. Consequently, considerably lower thermal stresses are expected in our laser and also, in this temperature range, the laser crystal is far away from its fracture limit. From this point of view, it can further be understood why a segmented crystal does not lead to improvements in the current operation regime while it might very well make sense to use it in materials which experience higher peak temperatures or lasers that are operated at higher pump powers.

To summarize, we presented compact Ho³⁺:YAG resonators with a homogeneous and segmented crystal with maximum output powers of 57.6 W and 51.9 W, respectively, at near-diffraction-limited beam quality. To find the maximum output power, the resonator mirrors and pump diameter have carefully been optimized to enable mode matched operation. In Q-switched operation, pulses with an energy of 1.14 mJ and a pulse width of 40 ns for the

Table 2 Lengths and relative doping concentrations of the optimized segmented crystal with regard to the homogeneous crystal

Segment number	1	2	3	4
Length share	0.25	0.25	0.25	0.25
Doping concentration	0.79	0.90	1.07	1.26

resonator with the homogeneous crystal (1.04 mJ and 50 ns for the resonator with the segmented crystal) have been demonstrated at a pulse repetition rate of 50 kHz. Interferometric measurements have been conducted to compare the thermal lens of the homogeneous and segmented crystal. In these experiments, the obtained temperature gradients of the homogeneous and segmented crystal have been very similar. Simulations of the presented optimized resonators have shown a good agreement between output power, beam profile, and beam quality factors. From the thermal simulations, longitudinal temperature profiles have been extracted and compared. As expected, the homogeneous crystal has shown a higher longitudinal peak temperature and larger longitudinal temperature gradient. The temperature distribution of the segmented crystal has not been as steady as expected from the initial design which could result from the simplified assumptions used during the design of the crystal. However, even an optimized segmented crystal with a steady temperature distribution has not surpassed the homogeneous crystal in the simulation. This has been explained by the effective position of the thermal lens inside the resonator which is closest to the center of the resonator in case of the homogeneous crystal and therefore, the stability limit is only reached at higher pump powers. We conclude that the use of segmented crystals only offers advantages in operation conditions where high temperatures are expected either by using high pump powers or by using materials which require pump schemes that lead to large quantum defects. Otherwise, the use of a homogeneous crystal with a carefully optimized resonator is the preferred alternative.

Acknowledgements We acknowledge the support of the mechanical workshop of the Fraunhofer IOSB and Artur Schander who fabricated special opto-mechanical components for the experimental setup.

Author contributions Katharina Goth wrote the main manuscript text. All authors reviewed the manuscript.

Funding Open Access funding enabled and organized by Projekt DEAL. Bundesministerium der Verteidigung.

Declarations

Conflict of interest The authors declare no conflict of interest.

Open Access This article is licensed under a Creative Commons Attribution 4.0 International License, which permits use, sharing, adaptation, distribution and reproduction in any medium or format, as long as you give appropriate credit to the original author(s) and the source, provide a link to the Creative Commons licence, and indicate if changes were made. The images or other third party material in this article are included in the article's Creative Commons licence, unless indicated otherwise in a credit line to the material. If material is not included in the article's Creative Commons licence and your intended use is not permitted by statutory regulation or exceeds the permitted use, you will need to obtain permission directly from the copyright holder. To view a copy of this licence, visit <http://creativecommons.org/licenses/by/4.0/>.

References

- O.L. Antipov, N.G. Zakharov, M. Fedorov, N.M. Shakhova, N.N. Prodanets, L.B. Snopova, V.V. Sharkov, R. Sroka, Cutting effects induced by 2 μm laser radiation of cw Tm:YLF and cw and Q-switched Ho:YAG lasers on ex-vivo tissue. *Medical Laser Appl* **26**(2), 67–75 (2011). <https://doi.org/10.1016/j.mla.2011.02.004>
- T.J. Carrig, in *Solid State Laser Technologies and Femtosecond Phenomena*, vol. 5620 (SPIE, 2004), pp. 187–198. <https://doi.org/10.1117/12.581962>
- I. Mingareev, F. Weirauch, A. Olowinsky, L. Shah, P. Kadwani, M. Richardson, Welding of polymers using a 2 μm thulium fiber laser. *Opt. Laser Technol.* **44**(7), 2095–2099 (2012). <https://doi.org/10.1016/j.optlastec.2012.03.020>
- P.A. Budni, L.A. Pomeranz, M.L. Lemons, C.A. Miller, J.R. Mosto, E.P. Chicklis, Efficient mid-infrared laser using 1.9- μm m-pumped Ho:YAG and ZnGeP₂ optical parametric oscillators. *J. Opt. Soc. Am. B* **17**(5), 723–728 (2000). <https://doi.org/10.1364/JOSAB.17.000723>
- M. Eichhorn, Quasi-three-level solid-state lasers in the near and mid infrared based on trivalent rare earth ions. *Appl. Phys. B* **93**(2), 269 (2008). <https://doi.org/10.1007/s00340-008-3214-0>
- E. Lippert, H. Fonnum, G. Arisholm, K. Stenersen, A 22-watt mid-infrared optical parametric oscillator with V-shaped 3-mirror ring resonator. *Opt. Express* **18**(25), 26475–26483 (2010). <https://doi.org/10.1364/OE.18.026475>
- F. Chen, M. Cai, Y. Zhang, B. Li, in *Fifth Symposium on Novel Optoelectronic Detection Technology and Application*, vol. 11023 (SPIE, 2019), pp. 946–950. <https://doi.org/10.1117/12.2521126>
- G. Liu, S. Mi, K. Yang, D. Wei, J. Li, B. Yao, C. Yang, T. Dai, X. Duan, L. Tian, Y. Ju, 161 W middle infrared ZnGeP₂ MOPA system pumped by 300 W-class Ho:YAG MOPA system. *Opt. Lett.* **46**(1), 82–85 (2021). <https://doi.org/10.1364/OL.413755>
- X.M. Duan, Y.J. Shen, B.Q. Yao, Y.Z. Wang, A 106W Q-switched Ho:YAG laser with single crystal. *Optik* **169**, 224–227 (2018). <https://doi.org/10.1016/j.ijleo.2018.05.094>
- D. Kracht, R. Wilhelm, M. Frede, K. Dupré, L. Ackermann, 407 W End-pumped Multi-segmented Nd:YAG Laser. *Opt. Express* **13**(25), 10140–10144 (2005). <https://doi.org/10.1364/OPEX.13.010140>
- R. Wilhelm, M. Frede, D. Kracht, Power Scaling of End-Pumped Solid-State Rod Lasers by Longitudinal Dopant Concentration Gradients. *IEEE J. Quantum Electron.* **44**(3), 232–244 (2008). <https://doi.org/10.1109/JQE.2007.911702>
- S. Hahn, M. Frede, J. Neumann, D. Kracht, in *Conference on Lasers and Electro-Optics* (Optica Publishing Group, 2009), p. CThR3. <https://doi.org/10.1364/CLEO.2009.CThR3>
- Q. Shen, X.Y. Cui, M.C. Yan, U. Eismann, T. Yuan, W.Z. Zhang, C.Z. Peng, Y.A. Chen, J.W. Pan, 11-watt single-frequency 1342-nm laser based on multi-segmented Nd:YVO₄ crystal. *Opt. Express* **27**(22), 31913–31925 (2019). <https://doi.org/10.1364/OE.27.031913>
- C. Evangelatos, P. Bakopoulos, G. Tsaknakis, D. Papadopoulos, G. Avdikos, A. Papayannis, G. Tzeremes, Continuous wave and passively Q-switched Nd:YAG laser with a multisegmented crystal diode-pumped at 885 nm. *Appl. Opt.* **52**(36), 8795–8801 (2013). <https://doi.org/10.1364/AO.52.008795>
- R. Wilhelm, D. Freiburg, M. Frede, D. Kracht, in *Quantum Electronics and Laser Science Conference* (Optica Publishing Group, 2006), p. JThC38. <https://doi.org/10.1109/CLEO.2006.4628494>
- R. Wilhelm, D. Freiburg, M. Frede, D. Kracht, End-pumped Nd:YAG laser with a longitudinal hyperbolic dopant concentration profile. *Opt. Express* **16**(24), 20106–20116 (2008). <https://doi.org/10.1364/OE.16.020106>

17. V. Magni, Multielement stable resonators containing a variable lens. *J. Opt. Soc. Am. A* **4**(10), 1962–1969 (1987). <https://doi.org/10.1364/JOSAA.4.001962>
18. W. Koechner, Thermal Lensing in a Nd:YAG Laser Rod. *Appl. Opt.* **9**(11), 2548–2553 (1970). <https://doi.org/10.1364/AO.9.002548>
19. D. Hanna, Astigmatic Gaussian beams produced by axially asymmetric laser cavities. *IEEE J. Quantum Electron.* **5**(10), 483–488 (1969). <https://doi.org/10.1109/JQE.1969.1075673>
20. M. Griesbeck, H. Büker, M. Eitner, K. Goth, P. Braesicke, M. Eichhorn, C. Kieleck, Mid-infrared optical parametric oscillator pumped by a high-pulse-energy, Q-switched Ho³⁺:YAG laser. *Appl. Opt.* **60**(22), F21–F26 (2021). <https://doi.org/10.1364/AO.424039>
21. M.E. Innocenzi, H.T. Yura, C.L. Fincher, R.A. Fields, Thermal modeling of continuous-wave end-pumped solid-state lasers. *Appl. Phys. Lett.* **56**(19), 1831–1833 (1990). <https://doi.org/10.1063/1.103083>
22. M. Rupp, M. Eichhorn, C. Kieleck, Iterative 3D modeling of thermal effects in end-pumped continuous-wave Ho³⁺:YAG lasers. *Appl. Phys. B* **129**(1), 4 (2022). <https://doi.org/10.1007/s00340-022-07939-z>
23. M.E. Wei, T.Q. Cheng, R.Q. Dou, Q.L. Zhang, H.H. Jiang, High-peak-power electro-optically Q-switched laser with a gradient-doped Nd:YAG crystal. *Opt. Lett.* **46**(19), 5016–5018 (2021). <https://doi.org/10.1364/OL.442131>

Publisher's Note Springer Nature remains neutral with regard to jurisdictional claims in published maps and institutional affiliations.